Published in final edited form as:
J Pathol. 2009 February ; 217(3): 362–371. doi:10.1002/path.2454.

Severe deficiency of coagulation Factor VII results in spontaneous cardiac fibrosis in mice

H Xu, **F Noria**, **MJ Sandoval-Cooper**, **H Menchen**, **DL Donahue**, **VA Ploplis**, and **FJ Castellino**

W.M. Keck Center for Transgene Research and the Department of Chemistry & Biochemistry, University of Notre Dame, Notre Dame, IN 46556, USA

Abstract

Mice genetically modified to produce low levels (~1% of wild-type) of coagulation FVII presented with echocardiographic evidence of heart abnormalities. Decreases in ventricular size and reductions in systolic and diastolic functions were found, suggestive of a restrictive cardiomyopathy, and consistent with an infiltrative myopathic process. Microscopic analysis of mouse hearts showed severe patchy fibrosis in the low-FVII mice. Haemosiderin deposition was discovered in hearts of these mice, along with increases in inflammatory cell number, ultimately resulting in widespread collagen deposition. Significant increases in mRNA levels of TGF-β, TNF-α and several matrix metalloproteinases in low-FVII mice, beginning at early ages, supported a state of cardiac remodelling associated with the fibrotic pathology. Mechanistic time course studies suggested that cardiac fibrosis in low-FVII mice originated from bleeding in heart tissue, resulting in the recruitment of leukocytes, which released inflammatory mediators and induced collagen synthesis and secretion. These events led to necrosis of cardiomyocytes and collagen deposition, characteristics of cardiac fibrosis. The results of this study demonstrated that hemorrhagic and inflammatory responses to a severe FVII deficiency resulted in the development of cardiac fibrosis, observed echocardiographically as a restrictive cardiomyopathy, with compromised ventricular diastolic and systolic functions.

Keywords

Animal models of human disease; gene-altered mice; coagulation; endothelium; cytokines; metalloproteinases; cardiomyopathy; systolic dysfunction; left ventricle; fibrosis; cardiac failure; vascular leakage; factor VII

Introduction

The extrinsic blood coagulation system is triggered by exposure of Tissue Factor (TF) to plasma through activation of blood cells and/or disruption of vascular integrity. The plasma protein, activated Factor VII (FVIIa), interacts with the exposed TF, initiating a cascade of reactions terminating in fibrin formation. Mice homozygous for targeted inactivation of the

Correspondence to: Dr. Francis J. Castellino, W.M. Keck Center for Transgene Research, 230 Raclin-Carmichael Hall, University of Notre Dame, Notre Dame, IN 46556, USA, Telephone: (574) 631-9152, Telefax: (574) 631-8017, fcastell@nd.edu.

Conflict of Interest: None for any author

Tissue Factor (coagulation factor III; F3) [1–3] or FVII (coagulation factor VII; F7) [4] genes do not survive the perinatal period. Because of these lethal phenotypes, mice expressing very low levels (~1% of levels in wild type (WT) mice) of these proteins have been generated [5, 6], and these mice survive to adulthood. In the case of low-expressing TF mice ($TF^{-/-}$ (hTg)), spontaneous bleeding and fibrosis was observed in heart tissue, with accompanying left ventricular (LV) dysfunction [5]. Haemosiderin deposition and fibrosis were also found in low-FVII mice ($FVII^{tTA/tTA}$) [5], but a characterization of $FVII^{tTA/tTA}$ mice in this regard has not been accomplished beyond this initial observation. No reports of cardiac fibrosis in mice accompanying total deficiencies of other haemostasis factors, *e.g.*, $FIX^{-/-}$ [5], have appeared, except for plasminogen activator inhibitor-1 (PAI-1)-deficient or urokinase-type plasminogen activator (uPA) overexpressing mice [7]. Whether this occurrence is related to a more exuberant fibrinolytic state is unknown.

To demonstrate relationships between fibrosis and the FVIIa/TF pathway, it is important to determine whether cardiac dysfunction occurred with deficiencies of the soluble ligand for TF, FVIIa, and to more completely characterize FVII-deficient mice with regard to this phenotype. Thus, we undertook a thorough study of $FVII^{tTA/tTA}$ mice over the course of a long portion of their lifespan, correlating mechanistic features of spontaneous bleeding, cardiac fibrosis, and heart dysfunction.

Methods

Mice

C57Bl/6 male mice producing ~1% of WT FVII were used [6]. All protocols were approved by the Institutional Animal Use and Care Committee.

Echocardiography

Mice were lightly sedated with 1.5% isoflurane inhalation to maintain their heart rates around 500 bpm. Echocardiography images were acquired using a Vevo 770 system (VisualSonics, Toronto, ON, Canada), with either a 30-MHz or 40-MHz transducer at a focal depth range of 12.7–6.0 mm, a temporal resolution of >150 frames/sec, and a spatial resolution <40 μm. Left ventricular (LV) diameters were measured using a parasternal short-axis view at the papillary muscle level. Pulsed-wave Doppler measurements were employed to analyze blood inflow at the mitral valve (MV), and outflow at the main pulmonary artery (PA), using a modified parasternal long-axis view. Calculations were made within the guidelines of the American Society of Echocardiography leading-edge convention [8]. A Doppler-derived determination of global cardiac function, combining systolic and diastolic parameters, *viz.*, the Total Ejection Isovolume Index (TEI-Index), was calculated using Doppler images at the levels of the mitral valve and ascending aorta [9].

Vascular permeability in the heart

Evans Blue (EB) dye was used to study vascular permeability in the heart. Retro-orbital injections of EB (5 μg/g of body weight) were administered at 4 and 2 days before sacrifice. Hearts were then removed for study.

Q-RT-PCR

Q-RT-PCR was performed using TaqMan chemistry with the primers and probes indicated in Table 1. Levels of mRNA were calculated using individual standard curves normalized to RPL19 [10].

Histology

Sections (4 μm) were prepared from fixed paraffin-embedded tissues, and stained with Gomori's (Prussian Blue) stain for iron, and Masson's trichrome or picro-Sirius red for collagen. Primary antibodies for immunohistochemical stains were rat-anti-mouse CD45 for leukocytes (PharMingen, San Jose, CA, USA), rat-anti-mouse Mac-3/F480 for macrophages (Serotec, Raleigh, NC, USA), and rat-anti-mouse P-Selectin for platelets (PharMingen). Double-labelling of endothelial cells (EC) and smooth muscle cells (SMC) was employed for vessel counting, using horseradish peroxidase conjugated rabbit-anti-human vWF (Dako) for EC, and mouse-anti-human α-smooth muscle actin (SMA; Sigma, St. Louis, MO)/NM-MHC SMemb (ABCAM, Cambridge, MA, USA) for SMC, as primary antibodies. For MMP-9 immunostaining, the primary antibody was rabbit-anti-mouse MMP-9 (ABCAM). {{Ed Query – please check last two sentences carefully for meaning}}.

Full details of our immunohistological procedures have been published [11, 12].

Brightfield image acquisition and morphometry

Brightfield images, compiling whole heart images, were acquired at a magnification of 200× using a Nikon Eclipse TE2000U microscope (Melville, NY, USA), with MicroPublisher 5.0RTV colour camera (QImaging, Burnaby, BC, Canada). Anti-CD45 and anti-macrophage images were analyzed for the number of cells per heart area using MetaMorph 7.0r3 software (Molecular Devices, Sunnyvale, CA, USA). Slides stained to detect haemosiderin were analyzed similarly for percent stain positive/heart area.

Vessel counts were obtained from a region of the anti-vWF/anti-SMC-stained LV of each heart. An area of the pericardium extending to the myocardium directly across from the midpoint of the right ventricle was photographed. For each heart, two sections from 4 mo WT mice, and 4 sections from 4 mo $FVII^{tTA/tTA}$, 12 mo WT, and 12 mo $FVII^{tTA/tTA}$ (approximately 80 μm apart in depth), were photographed with a SPOT-RT-SE camera (Molecular Diagnostics) for manual assessment of the number of positive vessels/heart area.

Epifluorescent image acquisition for collagen quantitation

A Photometrics Cascade 512B CCD camera (Roper, Tucson, AZ, USA) with a Texas Red (TR) fluorescent filter (Chroma, Rockingham, VT, USA) was employed for epifluorescent image acquisition. Thresholding for TR fluorescent-labelled images involved selecting the appropriate gray scale range of the pixels of interest in the positively stained region (collagen).

Transmission Electron Microscopy (TEM)

The LVs from WT and FVII$^{tTA/tTA}$ mice were fixed in Karnovsky's solution, post-fixed in OsO_4, and dehydrated in ethanol before embedding in plastic resins and sectioning, as we have described [13].

Statistics

Data are reported as mean ± SEM. Student's *t*-tests were performed using a value of $P \leq 0.05$ to reject the null hypothesis in two-tailed comparisons.

Results

Echocardiography

For echocardiographic measurements on lightly-anaesthesized mice, heart rates (HR) were not significantly different between age groups at the time of measurements, at 470–477 beats *per* minute (bpm) for the 4 mo mice and 494–506 bpm for the 12 mo mice. These HR are comparable to previous studies on echocardiography using C57Bl/6 mice, which show lower HR than other mouse strains [14]. Inhaled isoflurane was employed as the anaesthetic, since, in C57Bl/6 mice, this agent leads to minimal cardiac depression, as well as the most stable fractional shortening (FS) and end-diastole dimensions [14].

Initial indications of possible cardiac dysfunction in FVII$^{tTA/tTA}$ mice were noted by significantly increased heart weight (HW)/body weight (BW) ratios at necropsy of the FVII$^{tTA/tTA}$ mice compared to WT mice (Table 2). The generally reduced BWs of the FVII$^{tTA/tTA}$ mice are likely due to altered body development because of internal bleeding [6]. The greater HW in the FVII$^{tTA/tTA}$ mice, in view of their decreased BW, encouraged further study to assess whether increased heart volumes and/or increased wall densities account for the increased HW in the low-FVII mice.

Echocardiographic M-mode LV data using 4 and 12 mo WT and FVII$^{tTA/tTA}$ mice showed significant reductions in LV volume at diastole (LVV-d) between the FVII$^{tTA/tTA}$ and WT groups at both ages (Table 2). Additionally, substantial LV wall motion irregularities were found in the majority (6/8) of the FVII$^{tTA/tTA}$ mice examined. One of the more extreme examples of this is revealed by the M-mode echocardiogram of Figure 1, which shows severe reductions in systolic motion in both the posterior (PW) and anterior (AW) walls of the LV. This is reflected in the significant reductions in the Ejection Fractions (EF), Fractional Shortenings (FS), and Cardiac Outputs (CO), in both 4 mo and 12 mo FVII$^{tTA/tTA}$ mice (Table 2). Analyses of the transmitral flow by pulsed Doppler echocardiography were also indicative of a diastolic dysfunction in FVII$^{tTA/tTA}$ mice (Figure 1C,D; Table 2). The average early diastole/late atrial contraction (E/A) ratio that characterizes LV filling was significantly altered, also consistent with diastolic dysfunction. Tissue Doppler measurements around the mitral valve showed similar E/A values. Right-sided heart abnormalities were also present in 12 mo FVII$^{tTA/tTA}$ mice. Flow characteristics across the pulmonary valve (PV) of mice at 12 mo of age were estimated from pulsed Doppler examination of flow at the main pulmonary artery (PA) (Figure 1E,F). All velocities across

the PV were significantly reduced in FVII$^{tTA/tTA}$ mice, as was the PV-peak gradient (Table 2), reflective of the observed reduced CO.

A measure of mycardial performance that combines systolic and diastolic functions, *viz.*, the TEI-Index, has been used for assessment of global cardiac dysfunction [9]. The TEI-Index of the WT group was significantly increased in the FVII$^{tTA/tTA}$ mouse cohort (Table 2), thus confirming the severe LV systolic dysfunction in FVII$^{tTA/tTA}$ mice as early as 4 mo of age {{Ed Query please check meaning of this sentence}}.

Histological analysis of murine hearts

Histological analysis of 4 mo and 12 mo WT and FVII$^{tTA/tTA}$ mice showed spontaneous bleeding in hearts of low-FVII mice (Figure 2A–G). WT mouse hearts were devoid of haemosiderin (Figure 2A,D), whereas abundant haemosiderin deposition was seen throughout the myocardium in 4 mo FVII$^{tTA/tTA}$ mice, indicating previous bleeding (Figure 2B,E). Evidence that the haemosiderin resulted from phagocytosed red blood cells (RBC) is seen from an electron micrograph showing an extravascular RBC with electron dense iron engulfed by a macrophage (Figure 2C). Interstitial haemorrhages were further demonstrated by the presence of abundant widespread extravascular erythrocytes (Figure 2F,G) and platelets (Figure 2H,I) in the myocardia of low-FVII mice, many of which surrounded vessels. Blood leakage and cellular damage in heart tissue of 4 mo FVII$^{tTA/tTA}$ mice is dramatically illustrated by the gross photographic comparisons (Figure 2J,K) of EB leakage from blood into heart tissue of FVII$^{tTA/tTA}$ mice (Figure 2K), an effect absent in similarly-treated WT mice (Figure 2J).

CD45+ cells were scarce and scattered within the myocardia of 4 mo and 12 mo heart sections of WT mice (Figure 3A,C). In contrast, in FVII$^{tTA/tTA}$ mice of both ages, the majority of infiltrated CD45+ cells were localized on, and adjacent to, the pericardium (Figure 3B,D). In 4 mo WT mice, collagen was distributed only around heart vasculature (Figure 3E–G), as expected. However, in low FVII-mice (Figure 3H–J), collagen deposition extended from the pericardium into the myocardium, with some distribution near the endocardium, in both the LV and RV. Collagen deposition in hearts was significantly greater in 12 mo low-FVII mice than in WT mice (Figure 4A–E), and greater than that in 4 mo FVII$^{tTA/tTA}$ mice (Figure 3H–J). The collagen is clustered in areas of inflammatory cells.

Quantitative differences in CD45+ cells, hemosiderin, and collagen between hearts of 4 mo WT and FVII$^{tTA/tTA}$ mice are noted from the data of Figure 5A–C, and are significantly higher in the FVII$^{tTA/tTA}$ mice. That hemosiderin is the likely result of phagocytosis of RBC by macrophages is confirmed by the greatly increased macrophage counts in 4 mo FVII$^{tTA/tTA}$ heart tissue (Figure 5D), as compared to WT hearts, where no bleeding was observed.

vWF/SMC+ vessels were counted to compare the contributions of vessels to collagen levels (Figure 5E,F). Average vessel numbers in both 4 mo and 12 mo FVII$^{tTA/tTA}$ mice were greater than in WT mice, although these low numbers of vessels are not sufficient to significantly contribute to overall collagen levels in the severely fibrotic FVII$^{tTA/tTA}$ 12 mo mice.

Markers of fibrosis and ECM remodelling

Q-RT-PCR analyses of mRNA levels encoding some key proteins relevant to cardiac fibrosis revealed higher TNF-α mRNA levels in the hearts of 12 mo FVII$^{tTA/tTA}$ mice compared to WT mice (Figure 6A). Further, the abundance of MMP-2, MMP-3, MMP-9, and MMP-12 mRNA transcripts (Figure 6B–E) in the hearts of FVII$^{tTA/tTA}$ mice was higher than in WT mice hearts at both ages. TIMP-1 mRNA was also elevated in the hearts of FVII$^{tTA/tTA}$ mice compared to WT mice (Figure 6F), indicating this inhibitor of MMPs may be affecting dynamic matrix remodelling. To determine whether the higher mRNA levels of MMPs led to increased protein levels, immunohistochemical staining was employed for a key fibrotic response protease, MMP-9, in heart tissue of 4 mo mice. WT mice showed no detectable MMP-9 immunostaining (Figure 6G), whereas tissue from FVII$^{tTA/tTA}$ mice stained intensely for MMP-9 (Figure 6H). This increased MMP-9 level suggests that increased degradation of myocardial collagen and other components of the ECM was occurring. The significantly early enhanced level of TGF-β mRNA in FVII$^{tTA/tTA}$ mice (Figure 6I) further supported the finding of early development of cardiac fibrosis in low-FVII mice.

Temporal development of cardiac fibrosis in FVII$^{tTA/tTA}$ mice

To further determine the mechanistic events in the formation of fibrosis, we examined temporal relationships between bleeding, inflammation, and the development of heart fibrosis in the low-FVII mice. At 5 wk of age, FVII$^{tTA/tTA}$ mice showed normal histology of heart tissues. However, 1/7 of these FVII$^{tTA/tTA}$ mice showed intensive bleeding, as demonstrated by the accumulation of RBC and platelets outside the vessels and within the myocardium (Figure 7A,B). This area of bleeding was associated with abundant CD45+-leukocyte infiltration (Figure 7C). In contrast, this mouse presented neither haemosiderin nor collagen deposition (Figure 7D,E). Further investigations of mice at 6 wk of age showed 3 out of 4 mice had extensive bleeding (Figure 7F). Considerably increased CD45+-leukocyte infiltration was seen compared to the 5 wk mouse (Figure 7G). At 6 wk, cardiomyocytes showed massive necrosis, with many anuclear cells and loss of transverse striations (Figure 7F), but only faint indications of collagen staining (Figure 7H) and haemosiderin deposition (Figure 7I), suggestive of limited fibrosis at this age. Hearts of another three FVII$^{tTA/tTA}$ mice were examined at 8 wk of age. All of these had extensive haemosiderin deposition (Figure 7J), mostly distributed throughout the epicardium, and all hearts stained intensely for collagen (Figure 7K). These mice showed mature collagen deposition and fibrosis, but fewer RBC and diminished leukocyte infiltration (Figure 7L).

These studies support the hypothesis that vascular dysfunction leads to bleeding, which then initiates fibrosis. In support of this, TEM studies of 6 wk WT (Figure 7M,N) and FVII$^{tTA/tTA}$ mouse tissue (Figure 7O,P), revealed numerous abnormal blood vessels in cardiac tissue of the low-FVII mice. EC {{Ed Query define EC}} were branched throughout the cardiac tissue, migrating through cardiomyocytes (Figure 7O), and likely degrading the ECM, cell membranes, and the myofibrils that they encountered. RBC were found outside these abnormal vessels, suggesting that leakage from forming blood vessels had occurred (Figure 7O). In comparison, blood vessels in WT mice were found in interstitial spaces between cardiomyocytes, often surrounded by a conspicuous collagenous matrix (Figure

7M). Fibrotic areas of the LV in the low-FVII mice contained phagocytic macrophages and fibroblasts (Figure 7P). No extravascular blood cells were observed in the WT tissue (Figure 7 M,N).

Discussion

In this report, we have focused on heart pathophysiology as a site for expression of abnormalities involving the FVII system, using mice with a very low level of FVII. The significantly reduced EF, FS, and CO values in $FVII^{tTA/tTA}$ mice were consistent with advanced ventricular dysfunction; one explanation of which involves active inflammatory and fibrotic processes that result in ventricular stiffness, as was observed, which compromises filling. It has been proposed that in low-TF mice, mechanical disruption of vessels, and poor ability to achieve haemostasis in the low-FVII mice, compared to WT mice, led to bleeding and haemosiderin deposition [5]. However, this is mitigated by studies (data not shown) demonstrating that cardiac fibrosis is not observed in fibrinogen-deficient mice. Thus, other explanations have been sought.

The FVII/TF complex has been shown to elicit intracellular signalling through protease activated receptors (PARs) [15], leading to inflammatory responses that, in turn, can cause an imbalance of cytokines, *e.g.*, TGF-β, and damage to cardiomyocytes. To further distinguish these possible signalling effects from the bleeding events in causing cardiac fibrosis in $FVII^{tTA/tTA}$ mice, we performed mRNA analysis at time points sufficiently early (3 wk) such that cardiac fibrosis was not detectable by histological analysis in 3 wk $FVII^{tTA/tTA}$ mouse heart sections. The results showed similar levels of TGF-β and TNF-α, as well as MMP levels, in the $FVII^{tTA/tTA}$ mice as compared to WT mice. These results suggest that the observed inflammatory responses in the heart tissues, and the imbalance of protease activity in 4 mo and 12 mo $FVII^{tTA/tTA}$ mice, were secondary to the bleeding events.

Levels of profibrotic TGF-β were significantly higher in low-FVII mice than in WT mice at 4 mo of age, and this may lead to further activation and/or differentation of macrophages and fibroblasts, initiating collagen secretion that persists beyond 4 mo of age in low-FVII mice. Evidence of active remodelling of the ECM is provided by the increased mRNA levels for a variety of MMPs, in particular MMP-2 and MMP-9 proteases that are important participants in matrix remodelling and fibrillar collagen catabolism [16]. The transcript levels of MMP-3 and MMP-12 were also substantially increased at both timepoints in $FVII^{tTA/tTA}$ compared to WT mouse hearts, indicating the involvement of other ECM components in the process of fibrogenesis. Expression of the MMP inhibitor, TIMP-1, was also enhanced at the mRNA level in 12 mo mice, likely reflecting the dynamic state of ECM remodelling.

Studies of the time course of cardiac fibrosis suggested that this pathology was sequential. Bleeding and leukocytes appeared at 5 wk of age, continued at 6 wk, and diminished at 8 wk. Neither haemosiderin nor collagen deposition was found at 5 wk, but began at 6 wk, and matured at 8 wk. These events indicate that bleeding preceded leukocyte infiltration, and both bleeding and inflammation occurred prior to haemosiderin formation and collagen

deposition. Thus, cardiac fibrosis in FVII$^{tTA/tTA}$ mice originates from cardiac bleeding, which in turn recruits leukocytes into heart tissue. This inflammatory response then induces collagen synthesis and secretion, resulting in the observed necrosis of cardiomyocytes and collagen deposition, hallmarks of cardiac fibrosis.

FVIIa/TF, and resulting downstream proteases, can also provide non-haemostatic functions critical for maintaining the integrity of blood vessels by eliciting cellular signalling and EC function *via* PARs [15, 17]. Thus, cardiac fibrosis in FVII-compromised mice might result from defective vessels that are more likely to leak. The leaky vasculature, plus the impaired ability of FVII$^{tTA/tTA}$ mice to limit bleeding, can lead to excessive haemorrhage. This abnormal vasculature was demonstrated by the malformed, angiogenic-like vessels in FVII$^{tTA/tTA}$ mice at 6 wk of age, with RBCs found outside of these vessels, suggesting bleeding, followed by inflammation and collagen deposition.

In conclusion, this study supports a role for FVII in mouse heart that includes control of inflammation, microvascular bleeding, vessel integrity, and interstitial collagen deposition that would otherwise result in stiffness in heart ventricular walls. Thus, the ultimate result of a severe lack of FVII is massive cardiac fibrosis resulting in diastolic and systolic cardiac dysfunction.

Acknowledgments

We thank the staff of the Freimann Life Sciences facility for the breeding and husbandry of mice. This work was supported by grants HL013423 and HL073750 (to FJC) from the National Institutes of Health, and the Kleiderer-Pezold Professorship (to FJC)

References

1. Bugge TH, Xiao Q, Kombrinck KW, Flick MJ, Holmback K, Danton MJ, et al. Fatal embryonic bleeding events in mice lacking Tissue Factor, the cell-associated initiator of blood coagulation. Proc Natl Acad Sci USA. 1996; 93:6258–6263. [PubMed: 8692802]
2. Carmeliet P, Mackman N, Moons L, Luther T, Gressens P, Van Vlaenderen I, et al. Role of Tissue Factor in embryonic blood vessel development. Nature. 1996; 383:73–75. [PubMed: 8779717]
3. Toomey JR, Kratzer KE, Lasky NM, Stanton JJ, Broze GJ Jr. Targeted disruption of the murine tissue factor gene results in embryonic lethality. Blood. 1996; 88:1583–1587. [PubMed: 8781413]
4. Rosen E, Chan JCY, Idusogie E, Clotman F, Vlasuk G, Luther T, et al. Mice lacking Factor VII develop normally but suffer fatal perinatal bleeding. Nature. 1997; 390:290–294. [PubMed: 9384381]
5. Pawlinski R, Fernandes A, Kehrle B, Pedersen B, Parry G, Erlich J, et al. Tissue factor deficiency causes cardiac fibrosis and left ventricular dysfunction. Proc Natl Acad Sci USA. 2002; 99:15333–15338. [PubMed: 12426405]
6. Rosen ED, Xu H, Liang Z, Martin JA, Suckow M, Castellino FJ. Generation of genetically altered mice producing very low levels of coagulation Factor VII. Thromb Haemost. 2005; 94:493–497. [PubMed: 16268461]
7. Moriwaki H, Stempien-Otero A, Kremen M, Cozen AE, Dichek DA. Overexpression of urokinase by macrophages or deficiency of plasminogen activator inhibitor type 1 causes cardiac fibrosis in mice. Circ Res. 2004; 95:637–644. [PubMed: 15297377]
8. Lang RM, Bierig M, Devereux RB, Flachskampf FA, Foster E, Pellikka PA, et al. Recommendations for chamber quantification: a report from the American Society of Echocardiography's Guidelines and Standards Committee and the Chamber Quantification Writing Group, developed in conjunction with the European Association of Echocardiography, a branch of

the European Society of Cardiology. J Am Soc Echocardiogr. 2005; 18:1440–1463. [PubMed: 16376782]

9. Harjai KJ, Scott L, Vivekananthan K, Nunez E, Edupuganti R. The Tei index: a new prognostic index for patients with symptomatic heart failure. J Am Soc Echocardiogr. 2002; 15:864–868. [PubMed: 12221401]
10. Xu H, Ploplis VA, Castellino FJ. A coagulation factor VII deficiency protects against acute inflammatory responses in mice. J Pathol. 2006; 210:448–496.
11. Iwaki T, Cruz DT, Martin JA, Castellino FJ. A cardioprotective role for the endothelial protein C receptor in lipopolysaccharide-induced endotoxemia in the mouse. Blood. 2005; 105:2364–2371. [PubMed: 15528312]
12. Iwaki T, Sandoval-Cooper MJ, Brechmann M, Ploplis VA, Castellino FJ. A fibrinogen deficiency accelerates the initiation of LDL cholesterol-driven atherosclerosis via thrombin generation and platelet activation in genetically predisposed mice. Blood. 2006; 107:3883–3891. [PubMed: 16434491]
13. Ploplis VA, Cornelissen I, Sandoval-Cooper MJ, Weeks L, Noria FA, Castellino FJ. Remodeling of the vessel wall after copper-induced injury is highly attenuated in mice with a total deficiency of plasminogen activator inhibitor-1. Am J Pathol. 2001; 158:107–117. [PubMed: 11141484]
14. Roth DM, Swaney JS, Dalton ND, Gilpin EA, Ross J. Impact of anesthesia on cardiac function during echocardiography in mice. Am J Physiol Heart Circ Physiol. 2002; 282:H2134–H2140. [PubMed: 12003821]
15. Camerer E, Gjernes E, Wiiger M, Pringle S, Prydz H. Binding of factor VIIa to tissue factor on keratinocytes induces gene expression. J Biol Chem. 2000; 275:6580–6585. [PubMed: 10692465]
16. Saed GM, Zhang W, Diamond MP. Effect of hypoxia on stimulatory effect of TGF-beta 1 on MMP-2 and MMP-9 activities in mouse fibroblasts. J Soc Gynecol Investig. 2000; 7:348–354.
17. Kataoka H, Hamilton JR, McKemy DD, Camerer E, Zheng YW, Cheng A, et al. Protease-activated receptors 1 and 4 mediate thrombin signaling in endothelial cells. Blood. 2003; 102:3224–3231. [PubMed: 12869501]

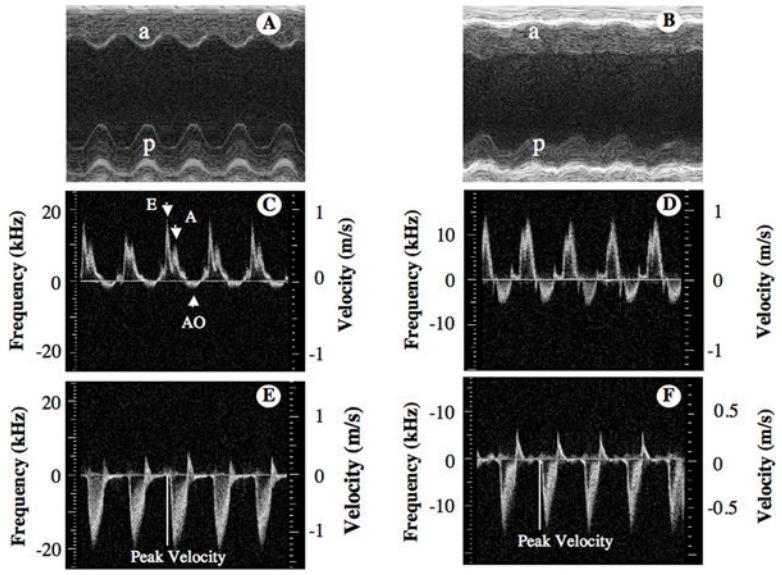

Figure 1.

Ultrasound evaluation of cardiac function in $FVII^{tTA/tTA}$ mice. Representative M-mode images from the short-axis view of the LV of 12 mo (A) WT and (B) $FVII^{tTA/tTA}$ mice. Anterior wall (a), posterior wall (p) wave motions. Doppler waveforms of the blood velocity obtained at the mitral valve level in (C) WT mice and (D) $FVII^{tTA/tTA}$ mice. AO refers to aortic outflow, E and A refer to early and late filling of the LV, respectively. (E, F) Doppler waveforms of the blood velocity at the main pulmonary artery in (E) WT and (F) $FVII^{tTA/tTA}$ mice. A white bar is indicated in each as a marker of the peak blood velocities.

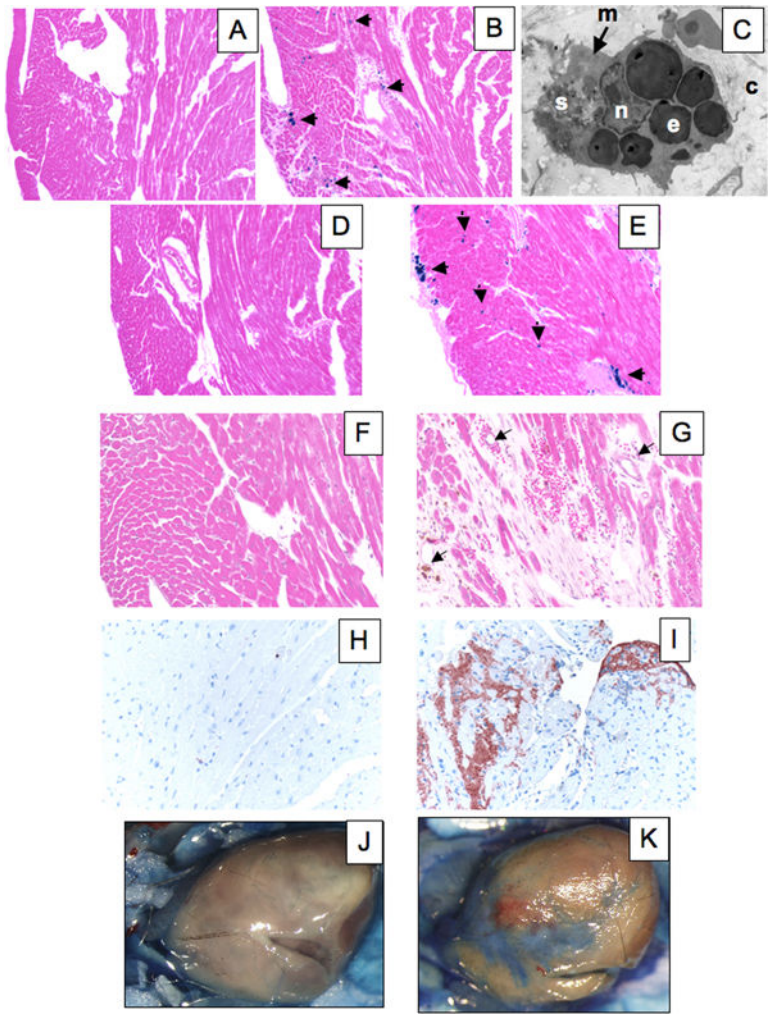

Figure 2.

Histochemistry and immunohistochemistry to detect spontaneous bleeding in hearts of low-FVII mice. (A,B) Prussian Blue staining (100×) of (A) WT) and (B) FVII$^{tTA/tTA}$ mice at 4. The arrows in B point to haemosiderin deposits (blue). (C) Electron micrographic detail (3500×) of a macrophage (arrow) from the LV in an area of a haemosiderin deposit in a 4 mo mouse heart section. Approximately 6 erythrocytes (an example is labeled e) containing electron-dense iron deposits are seen phagocytosed by the macrophage. Also crumpled membranes of an erythrocyte are observed in a nascent siderosome (s). A collagen-rich matrix (c) is also abundant in the area. The macrophage nucleus is labelled (n). (D, E) Prussian Blue staining (100×) of (D) WT and (E) FVII$^{tTA/tTA}$ mice at 12 mo. Haemosiderin deposits are clearly seen in E (blue). (F, G) H & E staining of heart tissue sections in 4 mo (F) WT and (G) FVII$^{tTA/tTA}$ mice (200× magnification). The arrows point to RBC surrounding vessels, showing leakage of blood into heart tissue in the FVII$^{tTA/tTA}$ mouse. (H, I) Bleeding is also evidenced by the positive (brown) immunostaining for P-selectin in heart tissue sections in 4 mo (I) FVII$^{tTA/tTA}$ mice, as compared to (H) control WT heart tissue (200×). (J, K) Gross photographs of hearts of (J) WT and (K) FVII$^{tTA/tTA}$ mice at 4

mo of age old after Evans blue injection. Photographs were taken at 6× magnification using a surgical dissecting microscope.

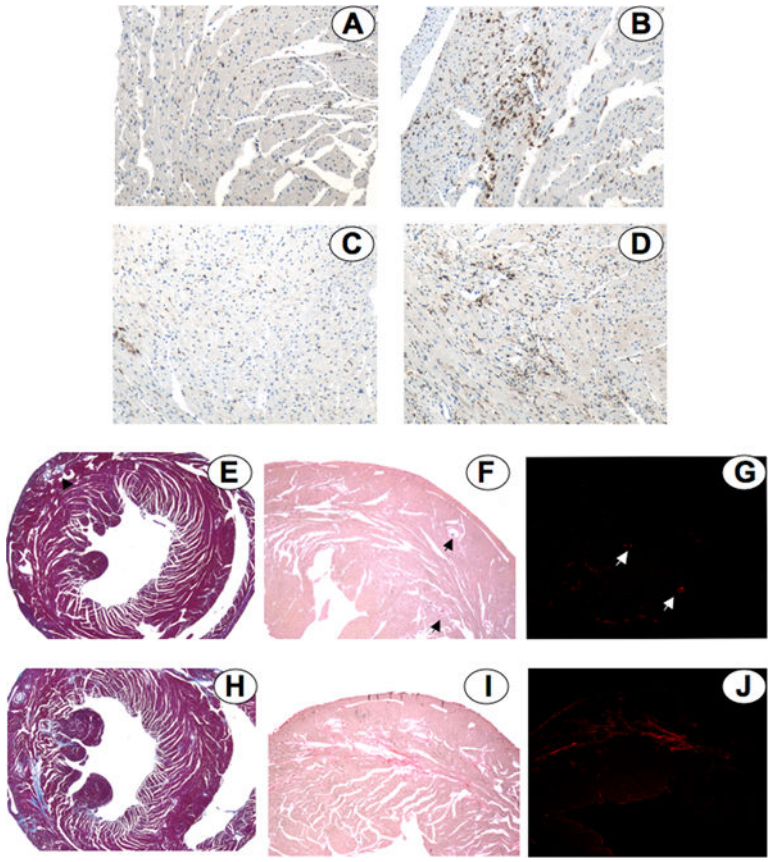

Figure 3.

Histological identification of cardiac inflammation and fibrosis in hearts of 4 mo $FVII^{tTA/tTA}$ mice. (A–D) Immunostaining for infiltrated CD-45+ cells (brown) in cardiac tissue. Panels A and B show anti-CD45 immunostains of 4 mo (A) WT and (B) $FVII^{tTA/tTA}$ mice (100×). Panels C and D display anti-CD45 immunostains (brown) of 12 mo (C) WT and (D) $FVII^{tTA/tTA}$ mice (100×). (E–J) Histological identification of collagen in hearts of 4 mo $FVII^{tTA/tTA}$ mice. Masson's trichrome staining of collagen (blue; 20×). Brightfield images of picro-Sirius Red staining (red) from 4 mo (F) WT and (I) $FVII^{tTA/tTA}$ (I) mice (60×). Epifluorescence detection (red) of collagen in hearts of 4 mo WT (G) and $FVII^{tTA/tTA}$ (J) mice hearts (40×). In E–G, the arrows point to collagen surrounding normal vessels.

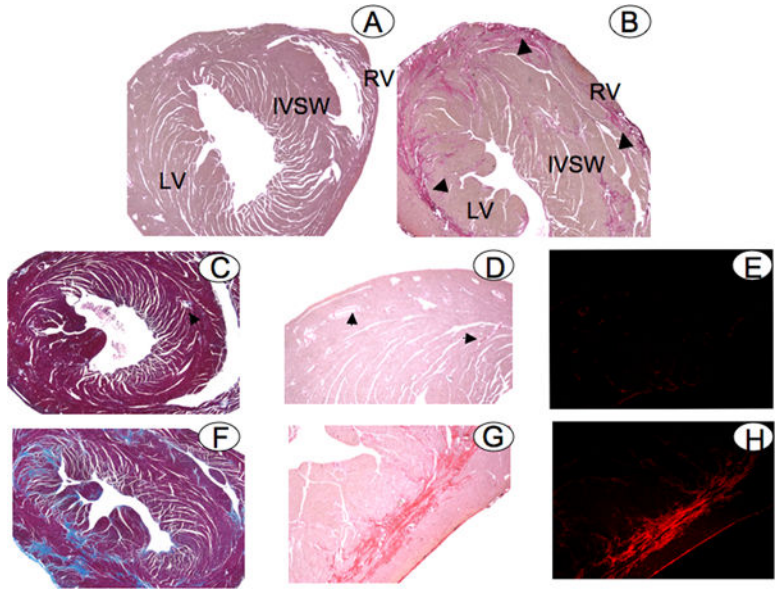

Figure 4.

Collagen deposition in hearts of 12 mo FVII$^{tTA/tTA}$ mice. Low-resolution brightfield images of picro-Sirius Red staining (red) in (A) 12 mo WT and (B) 12 mo FVII$^{tTA/tTA}$ mice. In B, the arrows indicate locations of some of the collagen deposits in the LV, RV and the interventricular septal wall (20×). Masson's trichrome staining of collagen (blue) in heart sections from (C) 12 mo WT and (F) 12 mo FVII$^{tTA/tTA}$ mice (20×). Higher resolution brightfield images of picro-Sirius Red staining (red) in (D) 12 mo WT and (G) 12 mo FVII$^{tTA/tTA}$ mice (60×). Epifluorescence detection (red) of collagen in hearts of (E) 12 mo WT and (H) 12 mo FVII$^{tTA/tTA}$ hearts (40×). In C, D, and E, the arrows point to collagen surrounding normal vessels.

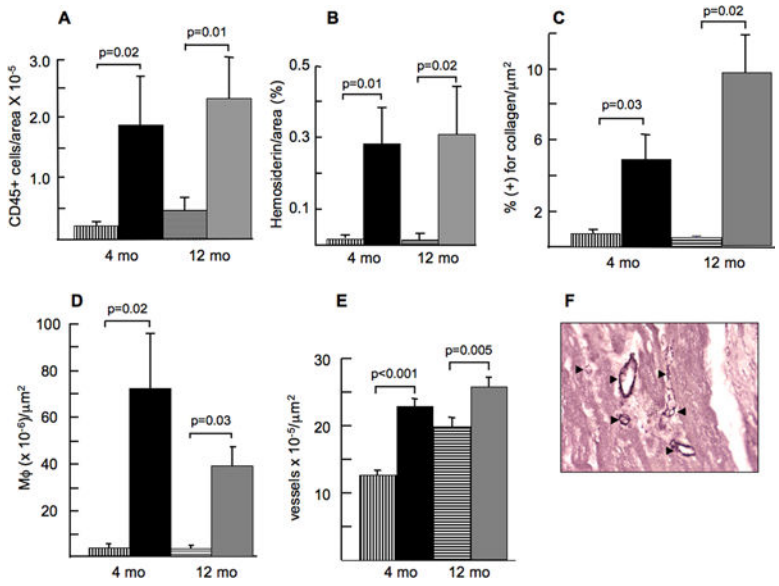

Figure 5.

Quantitative assessment of markers of cardiac inflammation, bleeding, and fibrosis in FVII$^{tTA/tTA}$ mice at 4 mo and 12 mo of age. (A) CD45, (B) haemosiderin, (C) collagen, (D) macrophage, (E) SMC+ vessel counts in the LV, with (F) an example of a 4 mo FVII$^{tTA/tTA}$ mouse heart section image (400×) used for counting. In this case, the arrowheads point to some of the vessels present. The quantitative data were obtained from morphometric analysis of histology sections (n = 6, 5, 4, and 4 hearts). At least 3 sections/mouse were counted for 4 mo WT, 4 mo FVII$^{tTA/tTA}$, 12 mo WT, and 12 mo FVII$^{tTA/tTA}$ counts, respectively.

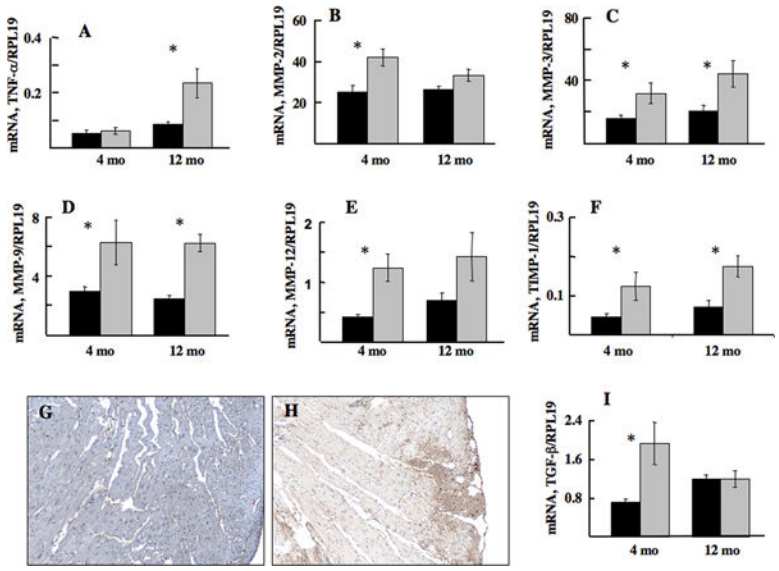

Figure 6.

Q-RT-PCR analysis of transcripts associated with tissue remodelling and fibrosis in $FVII^{tTA/tTA}$ mice. Results for mRNA levels of (A) TNF-α (B) MMP-2, (C) MMP-3, (D) MMP-9, (E) MMP-12, and (F) TIMP-1. (G and H) Immunohistochemical staining of MMP-9 in 4 mo of age (G) WT and (H) $FVII^{tTA/tTA}$ mouse hearts (100×). (I) Transcript levels of TGF-β in heart tissue. The black and grey bars represent values of WT and $FVII^{tTA/tTA}$ mice, respectively. Data are shown as the mean ± S.E.M, n = 5, for WT mice, and n = 6 for $FVII^{tTA/tTA}$ mice at 4 mo of age; n = 4 for WT and n = 4 for $FVII^{tTA/tTA}$ mice at 12 mo of age. *P<0.05.

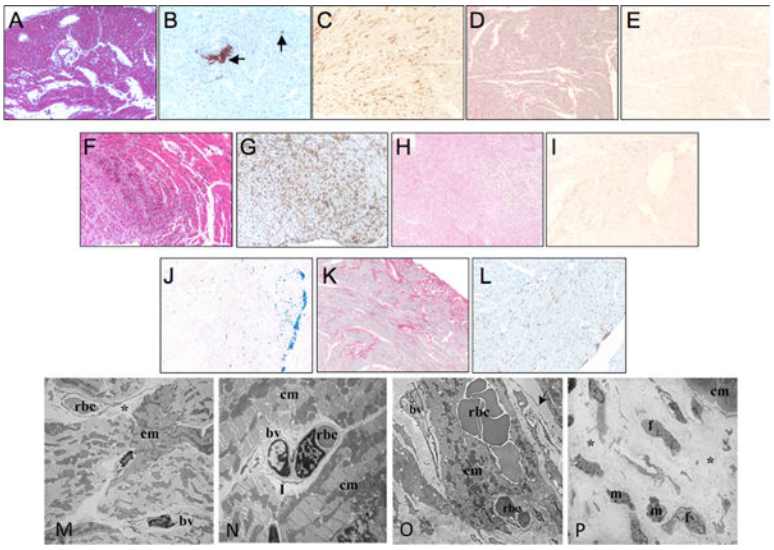

Figure 7.

Time course of development of cardiac fibrosis in FVII$^{tTA/tTA}$ mice. (A–E) Histology of FVII$^{tTA/tTA}$ hearts at 5 wk of age. (A) H&E staining (100×). (B) Anti-P-Selectin immunostaining (100×). The arrows point to platelet accumulation (brown). (C) Anti-CD45 staining (100×). Abundant brown-stained cells indicate CD45^{+}-leukocyte infiltration. (D) Picro-Sirius Red staining (100×). (E) Prussian Blue staining (100×). (F–I) Histology of FVII$^{tTA/tTA}$ hearts at 6 wk of age (100×). (F) H&E staining. (G) Anti-CD45 immunostaining (H) Picro-Sirius Red. (I) Prussian Blue. (J–L) Histology of FVII$^{tTA/tTA}$ hearts in 8 wk mice (100×). (L) Prussian Blue. (K) Picro-Sirius Red. (L) Anti-CD45 immunostaining for leukocytes. (M–P) TEM images of the LV of 6 wk of age WT (M and N) and FVII$^{tTA/tTA}$ (O and P) mice. (M) Intact blood vessels (bv) containing red blood cells (rbc) are seen in the ventricular parenchema within the collagenous matrix (*) in the WT specimen (2000×). (N) Active blood vessels (bv) are located in the interstitial space (I) between cardiomyocytes (cm) and do not modify the morphology of the cardiac cells (3500×). (O and P) The LV of FVII$^{tTA/tTA}$ mice. (O) Cardiomyocyte (cm)-containing RBC from a forming vessel. Extravascular RBC can also be seen in the area. An endothelial cell can be seen in recently formed vessels as well as endothelial cell processes (arrow) (3000×). (P) A fibrotic area of the LV. Macrophages (m) with included phagocytic vesicles after cell debris clearance and abundant fibroblasts (f) embedded in a rich collagenous matrix (*) are present. Cm surround the fibrotic areas (2500×).

Table 1

Q-RT-PCR primers and probes for quantification of mRNA levels

Target mRNA	Primers/Probes	Sequences (5′-3′)	Amplicon Size (bp)
MMP-2	FP	TGTTGGGGGAGATTCTCACTTTG	90
	RP	CCATCAGCGTTCCCATACTTTAC	
	Probe	AGCTGTGGACCCTGGGAGAAGGACA	
MMP-3	FP	GACGATGATGAACGATGGACAG	104
	RP	GCCTTGGCTGAGTGGTAGAG	
	Probe	TCCTGGTTGCTGCTCATGAACTTGGCCACT	
MMP-9	FP	CTCGAGGGCTTCCCTCTG	83
	RP	GGCCTTGGGTCAGGCTTAG	
	Probe	AGACGGCATCCAGTATCTGTATGGTCGT	
MMP-12	FP	GAGCAGTGCCCCAGAGG	80
	RP	ACGCTTCATGTCCGGAGTG	
	Probe	TGGATGAAGCGGTACCTCACTTACAGGATC	
TIMP-1	FP	CTGTGGGGTGTGCACAG	93
	RP	CCCACGAGGACCTGATCC	
	Probe	ACTGGAGAGTGACACTCACTGTTTGTGGA	
TIMP-4	FP	GCAAAGACCCTGCTGACAC	91
	RP	TGAATATCCTTGGCCTTCTCGAAC	
	Probe	ACTGATCCGGTATGAAATCAAACAGATAAAGATGT	
TGF-β	FP	CAGAAATATAGCAACAATTCCT	257
	RP	AAGGGCCGGTTCATGTCATGGA	
	Probe	TACAGGGCTTTCGATTCAGCGCTCACT	
TNF-α	FP	CCCCAAAGGGATGAGAAGTTC	100
	RP	GCTTGTCACTCGAATTTTGAGAA	
	Probe	TCATCAGTTCTATGGCCCAGACCCTCA	
PAI-1	FP	GACACCCTCAGCATGTTCATC	218
	RP	AGGGTTGCACTAAACATGTCAG	
	Probe	TCCTGCCTAAGTTCTCTCTGGAGACTGAAG	
RPL19	FP	ATGTATCACAGCCTGTACCTG	233
	RP	TTCTTGGTCTCCTCCTCCTTG	
	Probe	TTTCGTGCTTCCTTGGTCTTAGACCT	

FP, Forward primer; RP, reverse primer.

Table 2

Echocardiographic measurements of cardiac function of WT and FVII$^{tTA/tTA}$ mice[a]

Parameters[b]	WT	FVII$^{tTA/tTA}$	WT	FVII$^{tTA/tTA}$
	4 months		12 months	
HR	470 ± 103	477 ± 35	494 ± 73	506 ± 25
HW/BW (mg/g)	4.9 ± 0.2	5.9 ± 0.3*	4.7 ± 0.3	6.3 ± 0.7*
HW (mg)	149.6 ± 2.4	155.8 ± 3.2	183.1 ± 2.7	203.5 ± 7.6*
BW (g)	30.4 ± 1.7	26.5 ± 1.2	38.7 ± 2.6	32.5 ± 4.0*
M-Mode Measurements				
LVDs, mm	2.97 ± 0.13	2.92 ± 0.12	3.16 ± 0.15	3.04 ± 0.48*
LVDd, mm	4.13 ± 0.09	3.73 ± 0.09*	4.48 ± 0.15	3.91 ± 0.40*
LVVs, μL	35.5 ± 3.6	34.1 ± 3.2	39.8 ± 4.4	37.9 ± 13.6
LVVd, μL	76.2 ± 3.6	60.2 ± 3.2*	91.5 ± 7.2	67.9 ± 15.1*
LVSV, μL	40.7 ± 2.3	26.1 ± 1.1*	51.7 ± 5.0	30.0 ± 3.5*
LVEF, %	54.5 ± 3.4	44.8 ± 2.9*	56.4 ± 3.1	46.0 ± 4.0*
LVFS, %	28.4 ± 2.2	22.1 ± 1.6*	29.5 ± 2.1	22.8 ± 5.0*
CO, mL/min	19.8 ± 1.2	11.8 ± 0.6*	25.0 ± 1.4	14.0 ± 2.5*
TEI-Index	0.78 ± 0.09	1.05 ± 0.08*		
Doppler Measurements				
MV-E/A			1.47 ± 0.09	1.13 ± 0.17*
PA-PV, mm/s			1144 ± 146	751± 105*
PA-MV, mm/s			666 ± 84	429 ± 57*
PA-VTI, cm			3.95 ± 0.44	2.74 ± 0.33*
PV-PG, mm Hg			5.92 ± 1.41	2.55 ± 0.79*

[a] Values represent mean ± SEM, n = 8 for WT mice and n = 10 for FVII$^{tTA/tTA}$ mice at 4 mo of age; n = 4 for WT and n = 5 for FVII$^{tTA/tTA}$ mice at 12 mo of age.

* $P<0.05$ for pairwise comparisons between WT and FVII$^{tTA/tTA}$ mice.

[b] Table abbreviations: HR, heart rate; HW, heart weight; BW, body weight; LVD, end-systole LV diameter; LVDd, end-diastole LV diameter; LVSV, LV stroke volume; LVEF, LV ejection fraction; LVFS, LV fractional shortening; CO, cardiac output; MV-E/A, mitral valve E wave/A wave ratio; PA-PV; pulmonary artery-peak velocity; PA-MV; pulmonary artery mean velocity; PA-VTI, main pulmonary arterial velocity-time integral; PV-PG, pulmonary V peak gradient measured as outflow at the main pulmonary artery.